Digital and Gradient Refractive Index Planar Optics by Nanoimprinting Mesoporous Silicon

Anna L. Hardison, Tahmid H. Talukdar, Ivan I. Kravchenko, and Judson D. Ryckman*

We report the realization of digital and gradient index flat-optics and planar waveguides using the 'nanoimprinting refractive index' (NIRI) technique applied to mesoporous silicon. This technique combines the distinct optical and mechanical metamaterial qualities of mesoporous silicon, including its widely tunable effective refractive index and ability to undergo plastic deformation with a near zero Poisson ratio. Nanoimprinting with premastered and reusable stamps containing analog or digital features enables the continuous or discontinuous patterning of refractive index with high contrast $\Delta n \geq 0.8$ and subwavelength resolution. Using NIRI we experimentally demonstrate a wavefront shaping flat microlens array operating in the visible (405–635 nm) and mesoporous silicon and silica waveguides operating near 1310 nm. This study demonstrates the viability of patterning arbitrary refractive index distributions, $n(x,y)$, on the surface of a chip while circumventing the challenges and limitations of top-down lithographic techniques – thus opening a low-cost and scalable approach for the realization of advanced planar optical technologies.

1. Introduction

Nanostructured high refractive index materials offer a powerful means for tailoring the optical characteristics of planar optical components used in flat-optics,[1] metamaterials,[2] integrated photonics,[3–5] and transformation optics.[6,7] For many planar optical devices ranging from diffractive elements[8] and metalenses,[9–11] to optical cloaks,[7] waveguide-based devices,[3,4,12,13] and more, an ideal design solution is to engineer a sub-wavelength spacing between the dielectric elements, or in other words to construct a sub-wavelength grating (SWG) metama-

terial or effective medium. Attractively, the properties of SWGs are highly tunable and offer access to a wide range of effective refractive indices simply by varying the volume fractions of the constituent materials. However, SWGs are challenging to realize at optical frequencies as they demand subwavelength resolution. Modern approaches for planar SWG fabrication rely primarily on patterning dielectric surfaces through top-down subtractive or additive manufacturing techniques, many of which are expensive or difficult to scale, e.g., focused ion beam (FIB) milling and electron beam lithography (EBL),[4,14] or sacrifice pattern resolution in exchange for improved scalability, e.g. deep ultraviolet photolithography.[4,14]

On the other hand, bottom-up approaches based on self-organization phenomena occurring at the nano- or meso-scales offers a rapid, low-cost, and deeply subwavelength scheme for realizing effective medium SWGs and gradient refractive index (GRIN) profiles. In 1905 R. W. Wood described one of the earliest approaches for realizing a GRIN profile, referred to at the time as a "pseudo-lens", based on diffusing glycerin into a cylindrical slab of gelatin.[15] More recently, bottom-up refractive index control has been achieved by ionic exchange ($\Delta n \leq 0.1$),[16,17] in photothermorefractive glass ($\Delta n < 0.001$),[18] photo-annealed organic/inorganic hybrids ($\Delta n \approx 0.05$),[19] by electrospray printing of chalcogenide glass films ($\Delta n \leq 0.4$),[20] densification of Si or TiO_2 based nanocomposites in UV curable films ($\Delta n \leq 0.45$),[21,22] infrared glass-ceramics and nanocomposites ($\Delta n \leq 0.1$),[23–26] and electrochemically etched mesoporous silicon ($\Delta n \leq 2$)[27,28] and derivatives ($\Delta n \leq 0.5$).[29] Among these, mesoporous silicon, which features deeply subwavelength pore diameters in the range from ≈ 2 to 50 nm is especially attractive owing to its high index contrast and CMOS-compatible synthesis from silicon wafers.

Although a variety of bottom-up techniques exist for realizing tunable effective refractive indices, translating those self-organizing properties into functional devices with high index contrast Δn and patternable refractive index distributions $n(x,y)$ on the surface of a chip is a nontrivial task. Ion exchange on glass wafers patterned with a masking layer has been extensively studied and successfully commercialized to construct glass-based planar lightwave circuits,[17] however the index contrast ($\Delta n \leq 0.1$) and spatial resolution (≈ 2 µm) are both insufficient to construct compact flat-optical components and metasurfaces. Spatial refractive index control has been

A. L. Hardison, T. H. Talukdar, J. D. Ryckman
Holcombe Department of Electrical and Computer Engineering
Clemson University
South Carolina 29634, USA
E-mail: jryckma@clemson.edu
I. I. Kravchenko
Center for Nanophase Materials Science
Oak Ridge National Laboratory
Oak Ridge, TN 37831, USA

The ORCID identification number(s) for the author(s) of this article can be found under https://doi.org/10.1002/adom.202201597.

**ADVANCED
SCIENCE NEWS**

www.advancedsciencenews.com

**ADVANCED
OPTICAL
MATERIALS**

www.advopticalmat.de

demonstrated in infrared glass-ceramics and nanocomposites by local modification with laser,[25] thermal,[23,24] or photo-thermal treatments,[26] with an achievable index contrast up to $\Delta n = 0.1$. Another promising paradigm is to combine the bottom-up effective medium properties of mesoporous silicon with a secondary top-down patterning technique to spatially modulate the porosity and refractive index of the effective medium, e.g. by tuning electrochemical parameters in laterally etched microstructures ($\Delta n \leq 2$),[30] or programmatically loading the pores in 2D or 3D with a dielectric material such as a photoresin by direct laser writing ($\Delta n \approx 0.57$).[31] Alternatively, we have recently demonstrated that the porosity and refractive index of mesoporous silicon thin films could be modified by film compression in a process referred to as 'nanoimprinting refractive index' (NIRI).[32]

Here, we extend the NIRI approach to the patterning of digital and analog refractive index profiles $n(x, y) = n_0 + \Delta n(x,y)$ with subwavelength resolution. This is shown to enable the construction of functional digital and gradient refractive index photonic structures operating in the infrared and visible respectively. We demonstrate and characterize devices including optical waveguides fabricated using a digital stamp pattern and flat GRIN microlens arrays using an analog stamp profile. Our demonstration achieves analog, high-index contrast, and deep subwavelength control over the effective refractive index without requiring discretization or costly top-down lithographic techniques. Therefore, our NIRI technique provides a promising and scalable route toward realizing planar optical technologies with patterned digital or analog refractive index distributions which are otherwise challenging to produce by other methods.

2. Approach

Figure 1a depicts an overview of the NIRI patterning process, wherein a premastered and reusable stamp is utilized to compress mesoporous silicon and pattern the refractive index distribution $n(x,y)$. The NIRI process produces localized changes in refractive index through the permanent compression of the mesoporous silicon film (Figure 1b) which is characterized by a mixture of ductile-like pore wall bending and localized brittle fracture deformation modes.[33] Thus, nanoimprinting locally decreases film porosity from an initial value P_0 to a postimprint value P according to

$$P = 1 - \frac{1-P_0}{1-C} \tag{1}$$

where C describes the volumetric compression of the underlying film

$$C = -\frac{\Delta V}{V_0} \approx -\frac{\Delta h}{h_0} \tag{2}$$

which is determined by the engineering strain $\Delta h / h_0$ assuming uniaxial compression in the limit of a zero Poisson ratio (ZPR), $\nu \to 0$ (see supporting information for more details). Then the post-imprint porosity distribution $P(x,y)$ is related to the imprint profile according to
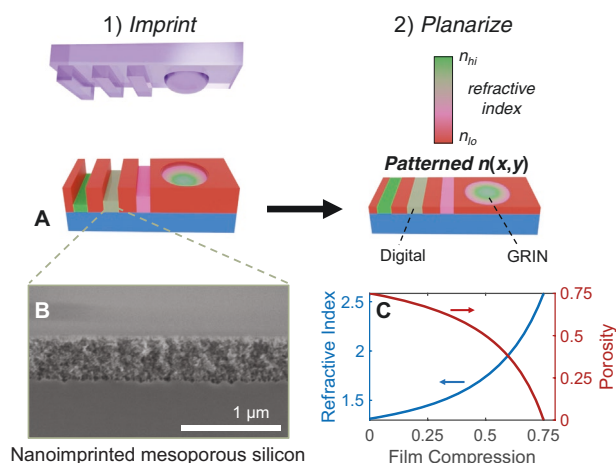

Figure 1. NIRI patterning overview. A) This diagram shows a simplified procedure for NIRI device fabrication (not to scale). Solid silicon or fused silica stamp is imprinted into the mesoporous silicon layer after electrochemical etching, patterning both topography and refractive index. Then the imprinted film may be polished to realize a flat-optical device with either digital or GRIN profiles. The areas in pink and green indicate a higher refractive index achieved through imprinting. B) SEM image of a post-imprinted mesoporous silicon film with film compression $C = 0.61$, C) model of the evolution of porosity P and effective refractive index n (at 635 nm) vs. film compression C assuming $P_0 = 0.75$ and a skeleton comprised of 50:50 Si:SiO$_2$.

$$P(x,y) = 1 - \frac{h_0}{h(x,y)}(1-P_0) \tag{3}$$

where the postimprint porosity and height distributions are bounded to $0 \leq P \leq P_0$ and $h_0(1-P_0) \leq h \leq h_0$. The effective medium properties after imprinting can be described by a Bruggeman effective medium model[27,32]

$$P(x,y)\frac{\varepsilon_1 - \varepsilon_{\text{eff}}(x,y)}{\varepsilon_1 + 2\varepsilon_{\text{eff}}(x,y)} + \left(1 - P(x,y)\right)\frac{\varepsilon_2 - \varepsilon_{\text{eff}}(x,y)}{\varepsilon_2 + 2\varepsilon_{\text{eff}}(x,y)} = 0 \tag{4}$$

where ε_1 is the dielectric constant of void, ε_2 is the effective dielectric constant of the skeleton, and $\varepsilon_{\text{eff}}(x,y)$ is the effective dielectric constant distribution of the film after imprinting which is related to the effective refractive index distribution according to $n(x,y) = \sqrt{\varepsilon_{\text{eff}}(x,y)}$.

As indicated in Figure 1c, the refractive index can be controlled over a wide working range Δn, readily reaching from ≈0.5-1 RIU at optical wavelengths (e.g. $\lambda_0 = 635$ nm) for a model assuming $P_0 = 0.75$ and a skeleton comprised of 50:50 Si:SiO$_2$.[32] As an example, Figure 1b shows an SEM cross-section of a mesoporous silicon film after nanoimprinting from an initial height of ≈1.14 μm to a final height of ≈0.44 μm, resulting in a film compression $C = 0.61$, and an estimated increase in refractive index $\Delta n = 0.85$ at $\lambda_0 = 635$ nm (supporting Figure S1, Supporting Information). The index contrast could also be subsequently modified by converting the film to mesoporous silica or otherwise modifying the pores if desired.[29] Within this framework, the mesoporous silicon thin films can be considered both an optical metamaterial, with widely tunable dielectric constant, as well as meso-scale mechanical metamaterial[34] which plastically deforms with approximately ZPR.
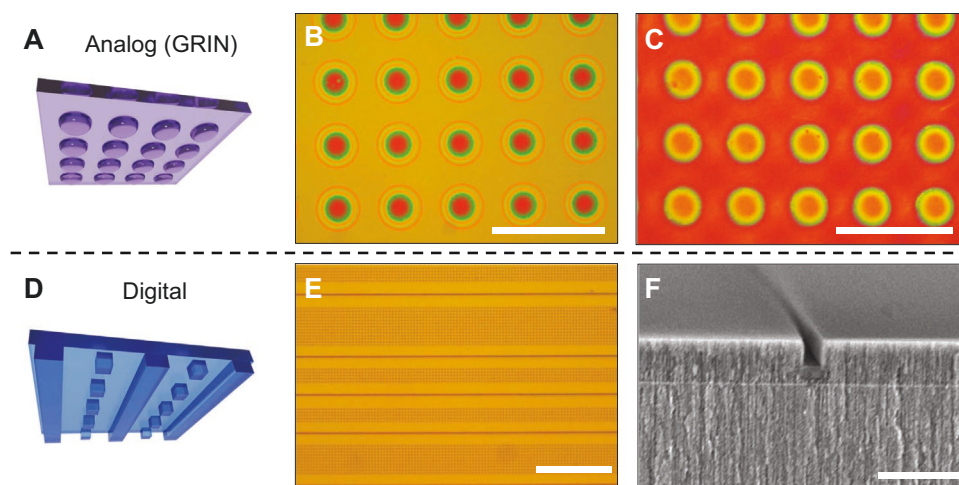
2201597 (2 of 7)

Figure 2. NIRI patterning of analog and digital refractive index profiles. A) An artistic rendering of an analog stamp profile in a fused silica microlens array stamp, B) an optical microscope image of the microlens array imprint in a ≈1.1 μm thick, ≈75% porosity film (scale bar 200 μm), C) a flat GRIN microlens array following 50 min CMP to a flat-optic thickness of ~320 nm prior to detachment from the substrate (scale bar 200 μm). D) An artistic rendering of a digital stamp profile used to fabricate waveguides, E) an optical microscope image of an imprinted waveguide sample (scale bar 100 μm), F) a cross-sectional SEM image of an imprinted waveguide following a secondary electrochemical etch to add low index waveguide cladding (scale bar 2 μm).

3. Results and Discussion

3.1. Flat GRIN Optics

To demonstrate the fabrication of flat GRIN $n(x,y)$ profiles, NIRI was performed using an analog stamp profile (**Figure 2**A) from an off-the-shelf 5 mm x 5 mm fused silica microlens array (SUSS MicroOptics) comprised of a rectangular array of spherical cap features with a radius of curvature equal to 708 μm and a pitch of 110 μm. Figure 2B shows an optical microscope

image of the analog profile formed in the nanoimprinted mesoporous silicon film after imprinting with a force of ≈4 kN for <5 sec. The gradient pattern can be directly observed from the concentrically uniform and radially modulated structural color profiles captured by the microscope camera. To quantitatively measure the imprinted $n(x,y)$ profile we performed multi-wavelength interferometry at wavelengths 450, 525, and 635 nm in a customized reflection mode microscope setup (see methods in supporting information). We then fit the experimentally observed fringe profiles (**Figure 3**A–C) to a model
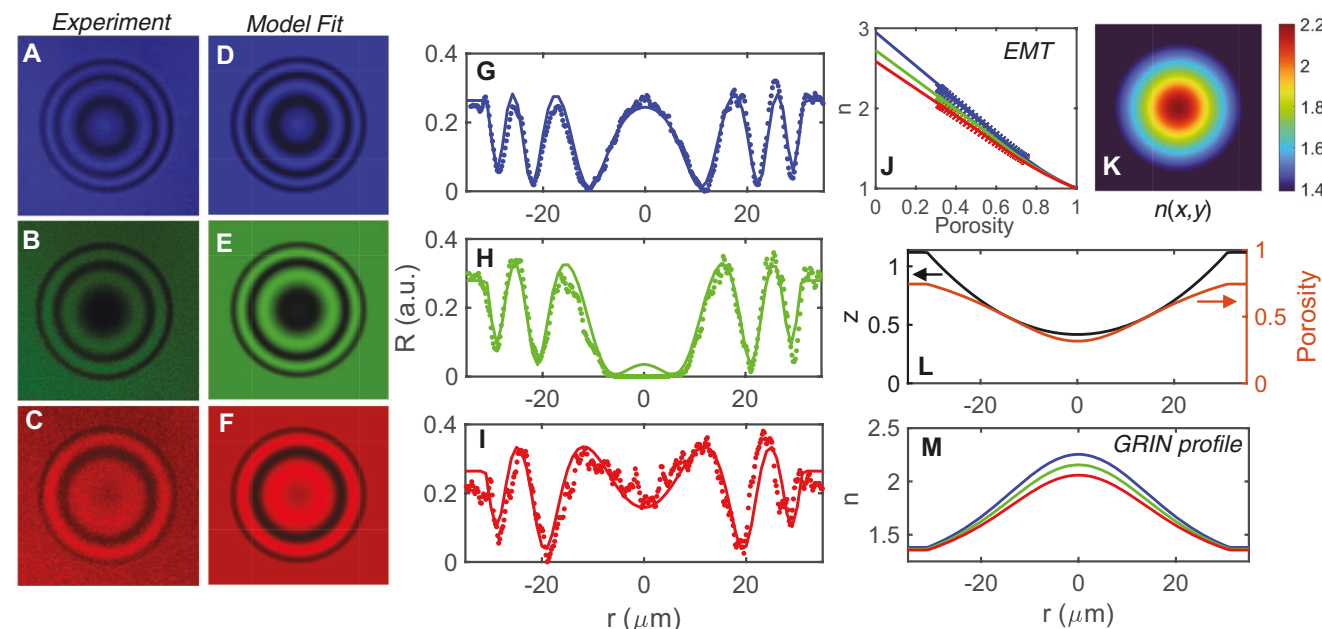

Figure 3. GRIN profile extraction. A–F) Experimental (A–C) versus modeled (D–F) fringe profiles of imprinted microlenses at wavelengths 450, 525, and 635 nm. G–I) 1D cross-section view of corresponding results in (A–F). J) effective medium theory (EMT) model (lines) and corresponding points (crosses) represented in the GRIN profile. K) Extracted 2D refractive index profile $n(x,y)$ at 525 nm, L) fitted porosity and height profiles, and M) comparison of the index profile at the red, green, and blue measurement wavelengths.

(Figure 3D–F) accounting for the patterned height $h(x,y)$ and dispersive gradient refractive index $n(x,y,\lambda)$ profiles. Our model fit shows excellent correspondence with the observed profiles as shown in Figure 3G–I, and indicates that the porosity of the patterned effective medium depicted in Figure 2B is modulated from ≈0.75 at the outer edge of the GRIN profile to ≈0.315 at the center as shown in Figure 3J,L. At the green test wavelength, this corresponds to an analog GRIN profile $n(x,y)$ patterned with a dynamic range from ≈1.35 to 2.15 over a radial distance of ≈30 μm. The extracted refractive index profile can be seen in Figure 3K,M, and is found to match a hyperbolic secant GRIN profile[35,36] of the form $n(r) = C_0\text{sech}(\alpha r) + n_0$ as indicated in supporting Figure S2, Supporting Information.

To realize a truly flat-optical structure capable of reshaping an incident wavefront according to its modulated refractive index profile $\Delta\phi(x,y) \propto \Delta n(x,y)$, we remove the imprinted surface topography by performing chemical mechanical polishing (CMP) and then transfer the patterned film from its silicon substrate to a transparent substrate (see supporting information and Figure S3, Supporting Information). Figure 2c shows an optical microscope image of a flat GRIN lens array after CMP was performed to planarize the NIRI patterned structure to an estimated thickness of ≈320 nm and prior to removal from the silicon substrate. Before performing CMP, the imprinted porous film was briefly annealed at 500 °C for 15 min in the air to make the surface less scratch-prone and to prevent film deformation during polishing. Under these conditions, a thin oxide layer is grown on the internal surface of the silicon skeleton which passivates the film, increasing its hardness and durability. Given the flat nature of the planarized film, the structural color pattern observed in Figure 2c arises from the patterned refractive index variation $\Delta n(x,y)$ modulating the local reflectance characteristics, which suggests NIRI could also be utilized to nanoimprint structural colors over a wide color gamut.

Next, we verify the wavefront shaping capabilities of the fabricated flat GRIN profiles. As shown in **Figure 4**A–C, the NIRI patterned flat-optics are predicted to behave as focusing microlens arrays. Each flat GRIN lens imparts a phase profile approximated by

$$\phi(r) \approx \frac{2\pi}{\lambda_0}\Delta n(r)t = \frac{2\pi}{\lambda_0}C_0\text{sech}(\alpha r)t \tag{5}$$

where the total phase coverage and focusing power of the lens are dependent on the index contrast Δn as well as the final polished film thickness t (Figure 3A-C). Assuming $\Delta n \approx 0.75$ to 1 in the visible region and $t = 320$ nm, the transmitted phase coverage achieved is on the order of π radians. Finite difference time domain (FDTD) simulations of this geometry and refractive index profile (Figure 3M) predict focusing an incident plane-wave to a full-width half-maximum (FWHM) of ≈12 μm at a focal length near ≈1.1 mm at $\lambda_0 = 635$ nm.

Experimentally we observe clear evidence of wavefront shaping and light focusing when collimated light is transmitted through the flat GRIN lens array as shown in Figure 4D, E. Measurements were performed by imaging the transmitted light using the setup described in the methods section and illustrated in supplementary information Figure S4, Supporting Information. Scanning in the z-dimension is performed by recording a video as the flat-optic is manually translated along the z-axis relative to the imaging objective (Video S1,
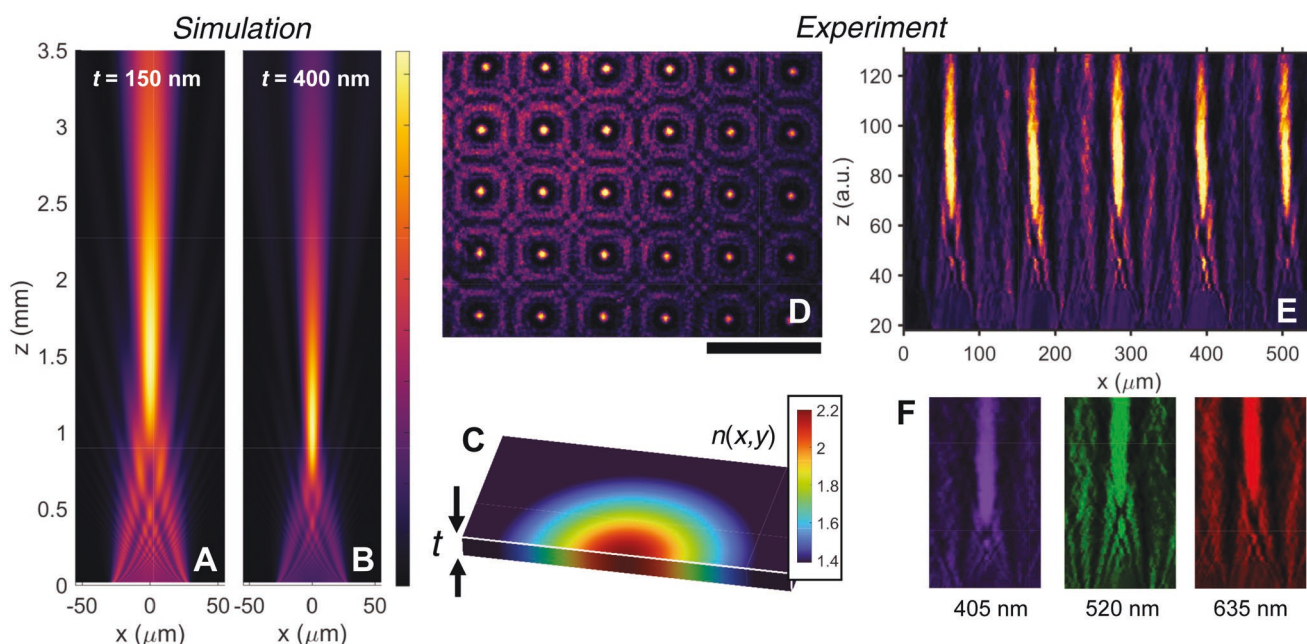

Figure 4. Flat GRIN microlens array demonstration. FDTD simulation of the flat GRIN lens operating at 635 nm for planar thicknesses: A) $t = 150$ nm or B) $t = 400$ nm. C) Illustration of the flat GRIN lens characterized with patterned index profile $n(x,y)$ and film thickness t. D) Experimental image of 635 nm light focusing after transmission through a ≈320 nm thick NIRI patterned GRIN microlens array (sample from Figure 2C, scale bar 200 μm), and E) corresponding z vs. x cross-section aggregated from video (Video S1, Supporting Information), and F) z versus x cross-section demonstrating wavefront shaping at visible wavelengths 405, 520, and 635 nm.

Supporting Information). Video scans are then post-processed to aggregate the video frames and construct a 2D cross-section (Figure 4E). Figure 4D shows a video frame where light is focused to a measured FWHM ≈13.5 µm at an operating wavelength $\lambda_0 = 635$ nm. The transmission efficiency of the GRIN microlens array was measured to be ≈74% as normalized to a transparent glass cover slide and is limited by absorption in the ≈5 µm thick mechanical support layer etched beneath the NIRI patterned film prior to detachment (Figure S5, Supporting Information). Scans were also captured for illumination wavelengths $\lambda_0 = 405$ nm and $\lambda_0 = 520$ nm, both of which exhibited similar light focusing behaviors as indicated in Figure 4F and Supporting Videos S2 and S3, Supporting Information. These results indicate the successful realization of a high index contrast, truly flat GRIN-optic with a smoothly varying (non-discretized) index profile and subwavelength thickness operating at visible frequencies.

3.2. Planar Optical Waveguides

In addition to patterning GRIN profiles we utilized NIRI to pattern digital refractive index patterns $n(x,y)$ as illustrated in Figure 2D–F. Specifically, we applied NIRI to pattern arrays of planar metamaterial waveguides, wherein nanoimprinting locally increases the refractive index of mesoporous silicon to form a high index waveguide core, followed by secondary anodization to prepare a low-index cladding (Figure S6, Supporting Information). NIRI was performed using a 3 mm x 2 mm area silicon stamp containing waveguide ridges of various widths ranging from 2 to 0.35 µm. As shown in the artistic rendering of the waveguide stamp (Figure 2D) and the microscope images of the imprinted pattern (Figure 2E), in the regions between

each waveguide the stamp pattern is filled with dummy pillar arrays. The purpose of these arrays is to increase the overall surface area of the stamp and to suppress long-range pattern density variations which could lead to non-uniform pressures and imprint depths. The stamps were prepared in silicon (see methods) by EBL, coated with ~10 nm of Cr, and etched by reactive ion etching to a depth of ≈1 µm.

Figure 2F shows a cross-sectional SEM image of an example 450 nm wide digital structure patterned with high fidelity. In this structure, an imprinted compression $C = 0.70$ is predicted to increase the effective refractive index by $\Delta n \approx 0.9$ in the near infrared. The low-index mesoporous silicon cladding layer, which was etched after imprinting, is also visible in this SEM image. SEM inspection indicates that etching resumes unimpeded by the densified porous film above and confirms that film integrity is retained after secondary anodization. While prior direct imprinting work has suggested the topographic direct imprinting resolution is limited only by the pore size,[37,38] in NIRI we expect the minimum patterning resolution to ultimately depend on the aspect ratio and the presence of mesoscale (≈10–50 nm) pore-wall bending in the lateral dimension, which coincides with a feature size dependent nonzero Poisson ratio in the case of isolated digital imprints (see supporting information and Figure S7, Supporting Information). In this work, we successfully imprinted line features as small as ≈350 nm in width to a high compression regime: $C \geq 60\%$ where $\Delta n \geq 0.8$, for an aspect ratio of ≈2.75:1.

We experimentally characterized NIRI patterned waveguides operating in the O-band from 1260 nm – 1360 nm using the experimental configuration depicted in Figure S8, Supporting Information. To enable input/output coupling the waveguide patterns were cleaved into ~1 mm long waveguide segments with exposed waveguide edge facets (**Figure 5**A). Mode simulation
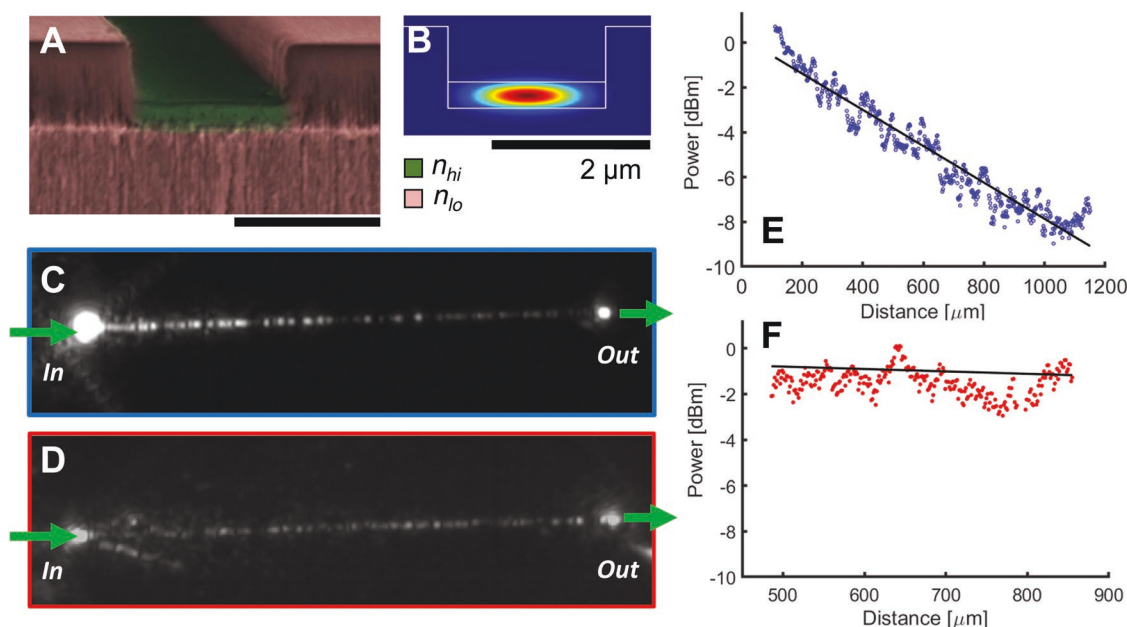

Figure 5. Nanoimprinted effective medium waveguides. A) Colorized cross-sectional SEM image of a 2 µm wide waveguide (2 µm scale bar), and b) simulated mode profile at 1310 nm using $n_{hi} = 2.19$ and $n_{lo} = 1.29$. Top view IR image of waveguide light scattering in the C) as-prepared mesoporous silicon waveguide, and D) oxidized mesoporous silica waveguide. Spectrally averaged power decay vs. distance for the E) as-prepared mesoporous silicon waveguide, and F) oxidized mesoporous silica waveguide.

assuming n_{hi} = 2.19 and n_{lo} = 1.29 (Ansys Lumerical) at 1310 nm shown in Figure 5B indicates that the fundamental quasi-TE polarized mode is well confined to the waveguide core. Infrared camera imaging of the transmitted waveguide mode aided fiber-to-chip coupling alignment optimization and was used to confirm modal quality (Figure S9, Supporting Information). As shown in Figure 5C–F waveguide propagation losses were characterized by infrared camera imaging (see supplementary methods). As prepared NIRI waveguides exhibited a propagation loss of 8.1 +/− 0.25 dB mm^{-1}, which is comparable with other reports of mesoporous silicon waveguides prepared by lithography and RIE in low resistivity p-type silicon.[39,40] Despite the clear presence of nonzero optical scattering visible in the infrared camera, the dominant loss mechanism is attributable to free-carrier absorption of the p-doped silicon skeleton. Assuming an acceptor concentration N_A = 3.2E18 to 8.5E18, the predicted free-carrier absorption coefficient of silicon at λ_0 = 1300 nm is estimated to be between 14.3 and 42 cm^{-1} for a silicon loss coefficient between 6 and 18 dB mm^{-1}.[41] Hence, a waveguide confinement factor in silicon near ≈0.5 is sufficient to attribute the majority of the observed propagation loss to free-carrier absorption rather than scattering loss. In the future, losses could be improved by lowering the free-carrier concentration to near intrinsic values, for example by compensation doping or by synthesizing mesoporous films by alternative processes such as metal-assisted chemical etching which are compatible with high resistivity silicon.[42]

The waveguide loss can also be improved by oxidizing the waveguide from mesoporous silicon into mesoporous silica. To ensure complete oxidation, NIRI patterned waveguide samples were thermally oxidized at 900 °C in the air for 24 h. In addition to eliminating free-carrier absorption, this process modulates the refractive index contrast of the waveguide which is bounded to material indices between air (n = 1) and SiO$_2$ (n = 1.45). Based on fitting the reflectance spectra of oxidized mesoporous silicon thin-film witness samples, we estimate the high and low refractive indices of our nanoimprinted mesoporous silica waveguides to be n_{hi} = 1.38 and n_{lo} = 1.15. Analysis of the oxidized waveguides showed a significant, roughly 8x, reduction in propagation loss. Due to the lower propagation losses and the influence from light scattering at the facets, our IR imaging-based analysis of oxidized samples was limited to the middle ≈500 μm portion of the waveguide (Figure 5F), limiting the measurement uncertainty to +/− 1 dB mm^{-1} and providing an estimated propagation loss of 1.1 +/− 1 dB mm^{-1}. In future work, measurements of longer mesoporous silicon waveguides can be used to estimate the waveguide loss with reduced uncertainty. Based on prior reports regarding mesoporous silica,[43] we anticipate surface-scattering limited losses below 1 dB cm^{-1} in the infrared and volume-scattering limited losses below 5 dB cm^{-1} in the visible should be feasible. This opens the prospect of using NIRI to fabricate low-cost photonic circuits, e.g. for single-use biosensor applications,[39,44] directly from silicon wafers without the need for lithography, etching, or costly silicon-on-insulator substrates.

4. Conclusion

NIRI patterning offers a scalable strategy for patterning refractive index on the surface of a chip while achieving high index contrast and subwavelength resolution. Unlike flat-optic technologies based on discretized local phase elements, meta-atoms, or 2D lithography, NIRI enables truly continuous control over the phase/index profile and is therefore a promising technique for enabling high-performance metasurfaces, analog Fourier surfaces, transformation optic components, structural colors, waveguide components, and other gradient index flat-optics. In future work, we envision NIRI could leverage 3D surface patterning to define custom reusable stamps to scalably fabricate fully customized digital or analog refractive index profiles which are otherwise challenging or impossible to achieve by other methods.

In addition to wavefront shaping, it has recently been shown that effective medium metasurfaces can simultaneously modulate amplitude by leveraging Fabry–Perot interference.[9] Consideration of the superstrate and substrate properties is therefore also important for controlling the local Fresnel transmission/reflection coefficients. While Equation (5) can be used in effective medium-based metasurface design, e.g. to generate multi-functional metasurfaces[45] or as a seed for inverse design optimization,[9] it remains an approximation and therefore future optimization of effective medium metasurfaces should leverage the combination of phase and amplitude modulation provided by nonzero Fresnel reflection coefficients.

Another consideration in future work is the birefringence of mesoporous silicon. In the present case, (100) derived mesoporous silicon exhibits uniaxial anisotropy and a polarization-independent response when illuminated at normal incidence. For planar waveguide applications or oblique incidence metasurface applications, however, the effective refractive index is polarization dependent[46] which provides an additional consideration and prospective design tool for polarization diverse applications. Similarly, polarization dependence could be achieved in normal incidence metasurfaces for (110) derived mesoporous silicon which exhibits biaxial anisotropy.[47] In such cases, we expect the magnitude of the birefringence to be modulated by film compression and degree of oxidation since the anisotropy is dependent on the pore morphology and index contrast.

Supporting Information

Supporting Information is available from the Wiley Online Library or from the author.

Acknowledgements

Conflict of Interest

The authors declare no conflict of interest.

Data Availability Statement

Keywords

[1] Z. Li, S. Yu, G. Zheng, *Nanophotonics* **2020**, *9*, 3699.

[2] S. Jahani, Z. Jacob, *Nat. Nanotechnol.* **2016**, *11*, 23.

[3] I. Staude, J. Schilling, *Nat. Photonics* **2017**, *11*, 274.

[4] P. Cheben, R. Halir, J. H. Schmid, H. A. Atwater, D. R. Smith, *Nature* **2018**, *560*, 565.

[5] A. Sharstniou, S. Niauzorau, A. L. Hardison, M. Puckett, N. Krueger, J. D. Ryckman, B. Azeredo, *Adv. Mater.* **2022**, *34*, 2206608.

[6] P. Markov, J G. Valentine, S M. Weiss, *Opt. Express* **2012**, *20*, 14705.

[7] J. Valentine, J. Li, T. Zentgraf, G. Bartal, X. Zhang, *Nat. Mater.* **2009**, *8*, 568.

[8] P. Lalanne, S. Astilean, P. Chavel, E. Cambril, H. Launois, *J Opt Soc Am A* **1999**, *16*, 1143.

[9] S. W. D. Lim, M. L. Meretska, F. Capasso, *Nano Lett.* **2021**, *21*, 8642.

[10] P. R. West, J. L. Stewart, A. V. Kildishev, V. M. Shalaev, V. V. Shkunov, F. Strohkendl, Y. A. Zakharenkov, R. K. Dodds, R. Byren, *Opt. Express* **2014**, *22*, 26212.

[11] A. Arbabi, Yu Horie, A. J. Ball, M. Bagheri, A. Faraon, *Nat. Commun.* **2015**, *6*, 7069.

[12] E. Luan, H. Yun, L. Laplatine, Y. Dattner, D. M. Ratner, K. C. Cheung, L. Chrostowski, *IEEE J. Sel. Top. Quantum Electron.* **2019**, *25*, 7300211.

[13] K. Hassan, J.-A. Dallery, P. Brianceau, S. Boutami, *Sci. Rep.* **2020**, *10*, 1123.

[14] V.-C. Su, C. H. Chu, G. Sun, D. P. Tsai, *Opt. Express* **2018**, *26*, 13148.

[15] R. A. Wood, *Physical Optics*, Macmillan, New York **1905**.

[16] C. Fourmentin, X.-H. Zhang, E. Lavanant, T. Pain, Y. Guimond, F. Gouttefangeas, L. Calvez, *Sci. Rep.* **2021**, *11*, 11081.

[17] J.-E. Broquin, S. Honkanen, *Appl. Sci.* **2021**, *11*, 4472 .

[18] O. M. Efimov, L. B. Glebov, L. N. Glebova, K. C. Richardson, V. I. Smirnov, *Appl. Opt.* **1999**, *38*, 619.

[19] S. Bachevillier, H.-K. Yuan, K. Tetzner, D. D. C. Bradley, T. D. Anthopoulos, P. N. Stavrinou, N. Stingelin, *Mater. Horiz.* **2022**, *9*, 411.

[20] S. Novak, P. T. Lin, C. Li, C. Lumdee, J. Hu, A. Agarwal, P. G. Kik, W. Deng, K. Richardson, *ACS Appl. Mater. Interfaces* **2017**, *9*, 26990.

[21] G. Yoon, K. Kim, D. Huh, H. Lee, J. Rho, *Nat. Commun.* **2020**, *11*, 2268.

[22] H. Hemmati, R. Magnusson, *Opt. Mater. Express* **2018**, *8*, 175.

[23] L. Sisken, C. Smith, A. Buff, M. Kang, K. Chamma, P. Wachtel, J. D. Musgraves, C. Rivero-Baleine, A. Kirk, M. Kalinowski, M. Melvin, T. S. Mayer, K. Richardson, *Opt. Mater. Express* **2017**, *7*, 3077.

[24] M. Kang, L. Sisken, C. Lonergan, A. Buff, A. Yadav, C. Goncalves, C. Blanco, P. Wachtel, J. D. Musgraves, A. V. Pogrebnyakov, E. Baleine, T. S. Mayer, C. G. Pantano, K. A. Richardson, *Adv. Opt. Mater.* **2020**, *8*, 2000150.

[25] M. Kang, L. Sisken, J. Cook, C. Blanco, M. C. Richardson, I. Mingareev, K. Richardson, *Opt. Mater. Express* **2018**, *8*, 2722.

[26] I. Mingareev, M. Kang, M. Truman, J. Qin, G. Yin, J. Hu, C. M. Schwarz, I. B. Murray, M. C. Richardson, K. A. Richardson, *Opt. Laser Technol.* **2020**, *126*, 106058.

[27] H. Sohn, in *Handbook of Porous Silicon*, Vol. *1*, (Ed: L. T. Canham), Springer International Publishing, Cham, Switzerland **2014**, p. 12.

[28] M. J. Sailor, *Porous Silicon in Practice: Preparation, Characterization, and Applications*, Wiley-VCH, Weinheim, Germany **2012**.

[29] C. R. Ocier, N. A. Krueger, W. Zhou, P. V. Braun, *ACS Photonics* **2017**, *4*, 909.

[30] N. A. Krueger, A. L. Holsteen, S.-K. Kang, C. R. Ocier, W. Zhou, G. Mensing, J. A. Rogers, M. L. Brongersma, P. V. Braun, *Nano Lett.* **2016**, *16*, 7402.

[31] C. R. Ocier, C. A. Richards, D. A. Bacon-Brown, Q. Ding, R. Kumar, T. J. Garcia, J. Van De Groep, J.-H. Song, A. J. Cyphersmith, A. Rhode, A. N. Perry, A. J. Littlefield, J. Zhu, D. Xie, H. Gao, J. F. Messinger, M. L. Brongersma, K. C. Toussaint, L. L. Goddard, P. V. Braun, *Light Sci Appl* **2020**, *9*, 196.

[32] T. H. Talukdar, J. C. Perez, J. D. Ryckman, *ACS Appl. Nano Mater.* **2020**, *3*, 7377.

[33] L. R. Meza, S. Das, J. R. Greer, *Science* **2014**, *345*, 1322.

[34] M. C. Fernandes, S. Mhatre, A. E. Forte, B. Zhao, O. Mesa, J. C. Weaver, M. Bechthold, K. Bertoldi, *Extreme Mech. Lett.* **2022**, *51*, 101549.

[35] Y. Li, G. Yu, B. Liang, X. Zou, G. Li, Su Cheng, J. Cheng, *Sci. Rep.* **2014**, *4*, 6830.

[36] W. Shao, H. Sato, X. Li, K. K. Mutai, Q. Chen, *Opt. Express* **2021**, *29*, 18932.

[37] J. D. Ryckman, M. Liscidini, J. E. Sipe, S. M. Weiss, *Nano Lett.* **2011**, *11*, 1857.

[38] J. D. Ryckman, Y. Jiao, S. M. Weiss, *Sci. Rep.* **2013**, *3*, 1502.

[39] T. H. Talukdar, G. D. Allen, I. Kravchenko, J. D. Ryckman, *Opt. Express* **2019**, *27*, 22485.

[40] G. A. Rodriguez, S. Hu, S. M. Weiss, *Opt. Express* **2015**, *23*, 7111.

[41] M. Nedeljkovic, R. Soref, G. Z. Mashanovich, *IEEE Photonics J* **2011**, *3*, 1171.

[42] F. Toor, J. B. Miller, L. M. Davidson, L. Nichols, W. Duan, M. P. Jura, J. Yim, J. Forziati, M. R. Black, *Nanotechnology* **2016**, *27*, 412003.

[43] P. Pirasteh, J. Charrier, Y. Dumeige, S. Haesaert, P. Joubert, *J. Appl. Phys.* **2007**, *101*, 083110.

[44] S. Aikio, M. Zeilinger, J. Hiltunen, L. Hakalahti, J. Hiitola-KeinäꞌꞌNen, M. Hiltunen, V. Kontturi, S. Siitonen, J. Puustinen, P. Lieberzeit, P. Karioja, *RSC Adv.* **2016**, *6*, 50414.

[45] T. H. Talukdar, J. D. Ryckman, *Opt. Express* **2020**, *28*, 30597.

[46] M. Fujii, J. Diener, "Optical Birefringence of Porous Silicon," in *Handbook of Porous Silicon*, (Ed: L. Canham), Springer International Publishing, Cham, Switzerland **2014**, pp. 245–253. https://doi.org/10.1007/978-3-319-05744-6_26.

[47] K. Hakshur, S. Ruschin, *Appl. Phys. Lett.* **2014**, *104*, 051909.